Physics in Medicine &
Biology

PAPER • OPEN ACCESS

Including medium effects and longer temporal scales in TRAX-CHEMxt

To cite this article: G Camazzola *et al* 2025 *Phys. Med. Biol.* **70** 245023

IOP Publishing Phys. Med. Biol. 70 (2025) 245023 https://doi.org/10.1088/1361-6560/ae29e1

Physics in Medicine & Biology

IPEM Institute of Physics and Engineering in Medicine

OPEN ACCESS

RECEIVED
12 September 2025

REVISED
14 November 2025

ACCEPTED FOR PUBLICATION
8 December 2025

PUBLISHED
18 December 2025

PAPER

Including medium effects and longer temporal scales in TRAX-CHEMxt

G Camazzola[1,2,3], D Boscolo[1,*], V Abram[4], E Scifoni[5], A Dorn[2], M Durante[1,6], M Krämer[1] and M C Fuss[7]

[1] Biophysics Department, GSI Helmholtz Centre for Heavy Ion Research GmbH, Planckstraße 1, 64291 Darmstadt, Germany
[2] Quantum Dynamics and Control Division, Max Planck Institute for Nuclear Physics, Saupfercheckweg 1, 69117 Heidelberg, Germany
[3] Department of Physics and Astronomy, Heidelberg University, Im Neuenheimer Feld 226, 69120 Heidelberg, Germany
[4] Department of Mathematics, University of Trento, Via Sommarive 14, 38123 Povo, Italy
[5] Trento Institute for Fundamental Physics and Applications (TIFPA), National Institute for Nuclear Physics (INFN), Via Sommarive 14, 38123 Povo, Italy
[6] Institute for Condensed Matter Physics, Technical University of Darmstadt, Hochschulstraße 6-8, 64289 Darmstadt, Germany
[7] Medical Physics Division, EBG MedAustron GmbH, Marie Curie-Straße 5, 2700 Wiener Neustadt, Austria
[*] Author to whom any correspondence should be addressed.

E-mail: d.boscolo@gsi.de

Keywords: TRAX-CHEMxt, Monte Carlo track structure, homogeneous chemical stage, ion radiation, radiation chemistry, antioxidants and biomolecules

Supplementary material for this article is available online

Abstract

Objective. Radiation biophysical modelling of the spatio-temporal events following energy deposition in a tissue-like medium is a useful tool for investigating mechanistic features of radiobiological processes. The present study focuses on the description of complex milieux and long time domains. *Approach*. Monte Carlo (MC) chemical track structure algorithms allow the formation, transport, and recombination of radical species under various irradiation conditions to be followed. This feature has been proposed to have outermost relevance, e.g. in the comprehension of the FLASH effect. Nevertheless, to extend the simulations predictability range in both temporal scales and realistic environments, while avoiding prohibitive running times, computationally lighter approaches have to be used in combination with the accurate step-by-step descriptions provided by MC. To this end, TRAX-CHEMxt has been implemented. *Main results*. We propose here an upgraded version of the code, capable now to investigate the chemical effects of radiation up to 1 s and in a more complex environment, featured not only by oxygenated water, but also by a representative biomolecule, RH, and an antioxidant component, XSH. The robustness of the code in this new configuration has been proven. Its predictions are compared with both full MC counterparts at the overlapping time scale, (1–10) μs, and available experimental data at longer temporal points, showing in all cases good agreements. The change in the chemical yields due to the presence of RH and XSH is then investigated, as a function of primary particle type, energy, LET, and target oxygenation. *Significance*. TRAX-CHEMxt can thus be effectively applied to study the impact of radiation-induced radicals at larger time scales on more complex systems, allowing for specific biological targets simulations.

1. Introduction

Damage contributions induced by various radiation qualities to biological targets can be grouped into two main categories. On one hand, the direct interaction between primary particles, with secondary electrons, and biomolecules. On the other hand, the indirect effect of intermediate-produced radicals following interaction with the solvent (i.e. water radiolysis), especially $OH^{\bullet}$, $H^{\bullet}$, and e^{-}_{aq}. The evolution of this 'indirect damage' at the track structure level can in turn be divided in various stages. Due to the initial

energy deposition by the radiation beam, ionised and excited water molecules, together with a substantial high amount of secondary electrons, are produced. The resulting species are highly unstable, and will then dissociate and thermalise with the surrounding environment until equilibrium is attained. Around 1 ps after the initial physical interactions, the products begin diffusing away from the track core and reacting with themselves. The initial dissociation of water in radicals and molecules is, however, quite independent on the primary radiation type (LaVerne 2000, Pastina and LaVerne 2001). Instead, the spatial location of the species determine their subsequent evolution (Boscolo *et al* 2018). During this 'heterogeneous' chemical stage, a non-uniform distribution of the chemical species is registered. The denser the track, the closer the produced radicals, and the more frequent the intratrack recombinations will be (Burns and Sims 1981). After around 1 μs, the species have dispersed from the core area of the track, and the actual 'track structure' dependence has become more loose. Henceforth—'homogeneous' biochemical stage—their reaction partners will principally be additional molecules present in the environment. These include not only biological targets, such as DNA, proteins, amino acids, nucleotides, and lipids, but also other important interacting species, like antioxidants (Meesat *et al* 2012), as glutathione (GSH), ascorbate ($AscH^-$, vitamin C), and superoxide dismutase (SOD). Nonetheless, this so-called homogeneous stage is, in fact, not entirely homogeneous in reality (Camazzola *et al* 2023). Rather, it exhibits a more continuous structure at the nanoscale level, with fewer localised clusters as compared to the previous stage.

From a chemical perspective, via the indirect action the radicals will react with generic biomolecules in the target (RH) through

$$OH^\bullet/H^\bullet/e^-_{aq} + RH \rightarrow R^\bullet + \text{side-products}, \tag{1}$$

inducing the creation of a damaged site, $R^\bullet$. This latter species can then be either repaired by the presence of enzymatic antioxidants (XSH) via hydrogen donation

$$R^\bullet + XSH \rightarrow RH + XS^\bullet, \tag{2}$$

or 'fixed' and made less repairable by the combination with oxygen (when present)

$$R^\bullet + O_2 \rightarrow ROO^\bullet. \tag{3}$$

The resulting peroxyl radicals $ROO^\bullet$, non-restorable forms of the original target molecules (Favaudon *et al* 2022), can in turn induce a peroxidation chain reaction, where hydrogen atoms are 'stolen' from other RH in a recursive way. Only the intervention of another antioxidant will block this loop, resulting in the formation of a stable organic hydroperoxide, ROOH. This may therefore be considered a potential indicator of the amount of harmed biological species

$$\begin{cases} ROO^\bullet + RH \rightarrow ROOH + R^\bullet & \text{(chain propagation)} \\ ROO^\bullet + XSH \rightarrow ROOH + XS^\bullet & \text{(chain termination)} \end{cases}. \tag{4}$$

Hence, a single species may be featured by multiple possible routes. For instance, $OH^\bullet$ can either react with other products from water radiolysis, can extract an electron from a target biomolecule, or can be scavenged by an antioxidant

$$OH^\bullet + XSH \rightarrow H_2O + XS^\bullet. \tag{5}$$

Simulations can be useful tools to inspect the kinetics of complex system's dynamics, since they provide temporal information regarding chemical species that are arduous to determine experimentally (Wasselin-Trupin *et al* 2002). Moreover, they can help testing hypotheses to understand several unexplained mechanisms, such as the FLASH effect (Favaudon *et al* 2014). The study of diffusion and reaction processes featuring radicals and molecules can be conducted through Monte Carlo (MC) track structure codes, focusing on an 'event-by-event' description of all single interactions happening in the target. For the high degree of precision and level of details provided, following all secondary electrons released from water molecules down to very low energies, the computing time can be high. This limits their applications to small volumes and to the description of track segments of the primary radiation. Most of currently available codes focus on oxygenated water environments (Boscolo *et al* 2020, Lai *et al* 2021, Zhu *et al* 2021, Hu *et al* 2022, Chappuis *et al* 2023). A more detailed overview on the current state of the art of track structure/analytical algorithms can be found in Camazzola *et al* (2023). For a more realistic description of the indirect damage on cells, the inclusion of biological components (Plante 2021), together with the coverage of longer time scales, is necessary. Due to high computational

costs, MC approaches alone are suboptimal to explore the biochemical stage. However, mathematical shortcuts can be exploited to reduce running times and extend simulations up to the domain of seconds. This is the direction where algorithms are moving at present time (Tran *et al* 2021, Favaudon *et al* 2022, Camazzola *et al* 2023, Chappuis *et al* 2023, Shin *et al* 2024, D-Kondo *et al* 2025).

The purpose of this study is to simulate how the interactions of chemical species with the biological environment are affected by initial particle quality, energy, LET, and target oxygenation. Both TRAX-CHEM (Boscolo *et al* 2018, 2020), chemical integration of the MC track structure code TRAX (Krämer and Kraft 1994, Wälzlein *et al* 2014), and its recent extension to the homogeneous stage TRAX-CHEMxt (Camazzola *et al* 2023), have been updated to account for the presence of additional background species. An extended time coverage, to 1 s, has been achieved as well, as reactions can happen even after some ms from the initial physical interactions (Shin *et al* 2024). After presenting the new features introduced in the code, section 2, the findings of the analyses are showcased in section 3. A detailed discussion of the outcomes can be found in section 4. To conclude, some investigations that can be performed by exploiting TRAX-CHEMxt are proposed in section 5.

2. Methods

2.1. Code description

Detailed descriptions of TRAX-CHEM and TRAX-CHEMxt can be found, respectively, in Boscolo *et al* (2018, 2020) and Camazzola *et al* (2023). In what follows, only a brief summary of the algorithms' major features is given.

TRAX-CHEM is a step-by-step MC code, able to simulate the stochastic and highly track-structure dependent initial chemical track evolution. It offers the possibility to score all single radicals' and molecules' positions produced around the primary particle track, at all times spanning from 1 ps to 1 μs, extending to 10 μs if necessary, at the expenses of higher calculation costs. Only when an acceptable degree of homogeneity is reached by the system (at around 1 μs), it is possible to 'switch' the information to a simplified and less computationally demanding procedure for simulating the chemical processes. TRAX-CHEMxt (Camazzola *et al* 2023) accomplishes so by employing an approach that utilises a continuous representation of the molecules' and radicals' locations as concentration distributions. They are assigned one per each species, and are derived by converting the spatial positions produced around the particle track. The tedious step-by-step procedure testing for possible reactions between all the combinations of individual reactants, together with their displacement in space, can now be replaced by a much faster set of differential equations. These describe both diffusion and reaction events, and are based on the respective one-dimensional, radial concentrations. A Crank–Nicolson scheme was applied to approximate the derivatives featuring the diffusion process (Fick's second law), while the explicit forward Euler method was exploited to describe the reactions (Camazzola 2024). The hypothesis of local homogeneity employed in the implementation of the algorithm, associated with the condensed information along the longitudinal direction (1D), is the foundation upon which the distributions are constructed.

From the pure computational point of view, the core of the algorithm is the chemical kinetics simulation of the environment under analysis, achieved by looping between reaction and diffusion events. Furthermore, the flatness of each concentration distribution is subject to periodic monitoring. This process is performed to speed up the computation, once a regime is reached where only reactions describe the system's dynamics. By selecting appropriate 'temporal steps' for the simulations, where temporal step denotes the virtual time of the simulation used to describe the evolution of the track, times exceeding 1 s can be reached. The small time step is, in fact, increased according to the interval covered. For instance, 1 ns samples the domain (1–10) μs, whilst 100 ns is exploited when computations exceed 1 s. As in the previous analysis (Camazzola *et al* 2023), the studies are performed under 'track segment' conditions, meaning that projectile LET and energy do not vary within the simulation volume. 'Track average' simulations on a MC base are prohibitive, due to the high computational costs required. Within the simulation settings, a cylindrical target is considered, with 5 μm radius and (1–10) μm height, depending on the primary particle LET. The projectiles are simulated as point sources, and directed towards the main axis at the centre of the cylinder. To guarantee secondary electrons equilibrium at the borders, thin water phantoms before and after the main one are also included.

The contributions of singular reaction channels to the overall increase (or decrease) of a chemical species can now be provided by TRAX-CHEMxt. These outputs need to be specified by the user, and have been introduced to infer the preferred production (or consumption) pathways featuring the desired radicals/molecules at specific time points. They provide information on how, when, and to which extent

Table 1. List of biological components and respective concentration values used in this work.

Biological component	Concentration (mM)	References
Proteins	10	Davies (2016), Hawkins and Davies (2019)
Amino acids	30	Piez and Eagle (1958), Davies (2016)
Nucleotides	3	Traut (1994)
RH	43	
Glutathione	3	Kosower and Kosower (1978), Wardman and von Sonntag (1995), Mikkelsen and Wardman (2003), Nauser *et al* (2015), Wardman (2022)
Ascorbate	1	Wardman and von Sonntag (1995), Nauser *et al* (2015), Wardman (2022)
XSH	4	

different reactions compete with one another (Cobut *et al* 2005), determining for instance the proportion of neutralisation versus damaging contributions of a specific radical.

2.2. Biological environment implementation

The simulation of a system mimicking the cellular environment is not trivial, due to the lack of consistency in literature (Shin *et al* 2024), to the enormous amount of different molecules present, and to their inhomogeneous distributions. Reactions in these solutions are very complex, and may depend on several parameters such as oxygen or antioxidant concentrations and medium acidity. To overcome this obstacle, in the present work, the biological environment is described through a 'generic' biomolecule RH and a 'generic' antioxidant XSH.

The list of biological components considered for the definition of RH and XSH, together with their respective concentration values, is summarised in table 1.

A concentration of 43 mM is assigned to RH, representing a cumulative effect of three categories: proteins, amino acids, and nucleotides. Proteins constitute roughly 70% of the dry mass of the organic material within the cell (Hawkins and Davies 2001, Liu and Gebicki 2012, Koch *et al* 2023). For their abundance and high reaction rate coefficients (Gebicki and Gebicki 1993, Liu and Gebicki 2012, Davies 2016, Hawkins and Davies 2019, Wardman 2022), they are deemed to be the main biological target of oxidation by primary water radicals. These are studied as monomer units, and their complete 3D structure is not accounted for. All orientations of the 3D molecules relative to the chemical species will occur, therefore as a first approximation their structure can be disregarded. The antioxidant scavenger XSH, instead, represents the contributions from glutathione and ascorbate, as performed in other studies (Colliaux *et al* 2011, Liu and Gebicki 2012, Nauser *et al* 2015), resulting in an overall concentration of 4 mM. Although being the most prominent small antioxidant molecules in a cellular system, their abundances vary significantly depending on the tissue considered (Liu and Gebicki 2012). Other enzymes such as SOD, catalase (CAT) and α-tocopherol (vitamin E) play also a role in the chemical reaction network. Nevertheless, these are featured by concentration values at least 3 orders of magnitude smaller than $GSH/AscH^-$.

Due to the limited amount of experimental data available, the determination of reaction rate constants is a particularly challenging process. Several reaction channels require relatively crude approximations or empirical derivations, as performed, e.g. in Tan *et al* (2023). The list of all reactions implemented in this work, together with the respective rate coefficients, can be found in table 2. The reaction constants κ featuring the oxygenated water environment are the same ones used in the previous analysis (Camazzola *et al* 2023), and can be found in the supplementary material of such work.

The orders of magnitude for primary water radicals with biomolecules are consistent with those reported in D-Kondo *et al* (2025), and in a similar fashion, it was decided to stop at the main stable products of reactions stemming from RH, without considering 'later generations'. As reported by Liu and Gebicki (2012) in the context of protein peroxidation, it is indeed challenging to ascertain which specific (protein) site reacts with the primary water radicals, and to understand the subsequent dynamics, through experimental means. Consequently, only global damages, such as ROOH yields, can be quantified. Following the same logic, the products of the reactions with XSH, i.e. $XS^\bullet$, HS^-, and $X^\bullet$, are not followed, and attention is given just to the first-order neutralisation mechanisms. Concurrently, certain approximations are made with regard to the reaction products. Some species from table 2, such as H_2 and OH^- in reaction (xxxiii), have been introduced in accordance with stoichiometric principles (mass

Table 2. List of reactions and respective reaction rate constants assumed for the biological environment. The κ values are determined under normal conditions, i.e. neutral pH and 25 °C. The numbering sequence continues that used for the oxygenated water scenario (cf table SM1 in the supplementary materials).

	Reaction	κ [10^{10} dm^3 mol^{-1} s^{-1}]	References
(xxvii)	$OH^\bullet + RH \rightarrow R^\bullet + H_2O$	0.1	Michaels and Hunt (1978), LaVerne and Pimblott (1993), Huie (2003), von Sonntag (2006), Liu and Gebicki (2012)
(xxviii)	$R^\bullet + O_2 \rightarrow ROO^\bullet$	0.023	Neta *et al* (1990), Hawkins and Davies (2001, 2019), von Sonntag (2006), Liu and Gebicki (2012), López-Alarcón *et al* (2014), Nauser *et al* (2015)
(xxix)	$R^\bullet + R^\bullet \rightarrow R_2$	0.01	Davies (2016), Leinisch *et al* (2017), Labarbe *et al* (2020)
(xxx)	$R^\bullet + ROO^\bullet \rightarrow ROOR$	0.01	Leinisch *et al* (2017), Labarbe *et al* (2020)
(xxxi)	$ROO^\bullet + RH \rightarrow ROOH + R^\bullet$	0.000 05	Neta *et al* (1990)
(xxxii)	$ROO^\bullet + ROO^\bullet \rightarrow ROOR + O_2$	0.01	Neta *et al* (1990), Huie (2003), Wardman (2022)
(xxxiii)	$e^-_{aq} + RH + H_2O \rightarrow H_2 + R^\bullet + OH^-$	0.05	Michaels and Hunt (1978), Huie (2003), von Sonntag (2006)
(xxxiv)	$H^\bullet + RH \rightarrow H_2 + R^\bullet$	0.001	Michaels and Hunt (1978), LaVerne and Pimblott (1993), Huie (2003), von Sonntag (2006)
(xxxv)	$OH^\bullet + XSH \rightarrow XS^\bullet + H_2O$	1	von Sonntag (2006), Davies (2016), Labarbe *et al* (2020), Tan *et al* (2023)
(xxxvi)	$e^-_{aq} + XSH \rightarrow HS^- + X^\bullet$	0.3	Huie (2003)
(xxxvii)	$H^\bullet + XSH \rightarrow H_2 + XS^\bullet$	0.7	Colliaux *et al* (2011)
(xxxviii)	$R^\bullet + XSH \rightarrow RH + XS^\bullet$	0.0005	Huie (2003), von Sonntag (2006), López-Alarcón *et al* (2014), Labarbe *et al* (2020), Wardman (2022)
(xxxix)	$ROO^\bullet + XSH \rightarrow ROOH + XS^\bullet$	0.00 005	Neta *et al* (1990), Huie (2003), Labarbe *et al* (2020), Wardman (2022)

Table 3. List of diffusion coefficients featuring the biological environment.

Species	D [10^{-9} m^2 s^{-1}]	References
RH & products	0.6	Boyer and Hsu (1992), Ma *et al* (2005), Torres *et al* (2012), Wang *et al* (2012), Romero *et al* (2019), Yu *et al* (2019), Miyamoto and Shimono (2022), Tang *et al* (2022)
XSH & products	1	Stricks and Kolthoff (1952), Shamim and Baki (1980), Jin and Chen (2000), Ganesh *et al* (2018), Soriano *et al* (2018)

conservation). While the biological products like $R^\bullet$ are consistently generated, the vast plethora of possible byproducts depends on the specific biomolecule under examination Koch *et al* (2023). To conclude, a remark is due for reaction (xxviii): in literature (see table 2) consistent values of $1 \cdot 10^9$ dm^3 mol^{-1} s^{-1} are reported for oxygen depletion from protein radicals, but no reliable data exists for amino acids and nucleotides. Therefore, the final κ is derived from a weighted mean, with the scaling coefficient derived from the ratio between proteins and overall RH concentrations. Nevertheless, the ultimate yield of $ROO^\bullet$—and ROOH—was found to strongly depend on this reaction rate, even under small variations in its value. A sensitivity analysis is presented in section 4.3.

Diffusion coefficients are assigned both to the major reactants, RH and XSH, and all respective products. These are summarised in table 3.

The final value for RH is derived from a weighted mean, computed in the same manner as the one described above to get the κ for reaction (xxviii) in table 2. It has been rounded up also to partially offset the fact that the algorithm treats only point-like radicals, implying that the migration of damaged sites along the molecule (Liu and Gebicki 2012)—intramolecularity effect—that results in an increased mobility, can not be directly considered. Diffusion coefficients for both GSH and $AscH^-$, instead, are found to be quite similar. The majority of collected values are experimentally derived under water conditions. They are preferred, for consistency with the other chemical species, and because the entire calibration and validation process in TRAX-CHEM has been performed in H_2O. The introduction of a viscous environment would have necessitated significant modifications, already at the dissociation/thermalisation level during the physico-chemical stage.

From the computational point of view, the two new scavengers are treated as homogeneously distributed (Michaels and Hunt 1978, Autsavapromporn *et al* 2007, Labarbe *et al* 2020, Plante 2021, Wardman 2022, D-Kondo *et al* 2025), in the same manner as oxygen (Boscolo *et al* 2020). This means that their concentrations are large enough to maintain their values constant throughout the simulation, and at the same time sufficiently lower than that of water to avoid direct interaction with the primary ionising radiation (Colliaux *et al* 2011, Ramos-Méndez *et al* 2020, Chappuis *et al* 2023). For the homogeneous stage simulated with TRAX-CHEMxt, this resulted in a simple update of the reaction network scheme and the pool of simulated species. For the heterogeneous chemical stage (MC), the introduction of the new scavengers required substantial modifications at the code level. The reaction probabilities are defined in the same way as for O_2. However, a selection procedure needs to be introduced. The probability of a reaction between a radical and a specific scavenger (if applicable) can be expressed as P_{O_2}, P_{XSH}, and P_{RH}. All the probabilities are considerably less than 1, such that their sum is lower as well. Concurrently, the radical can also interact with other species surrounding it. For each time step, only one reaction pathway can occur, in a sort of 'competition' between the other reactants, and it is not granted than the radical will react at all. Hence, for each simulation loop, a random number is extracted, x, to assign to the radical its possible reaction partner:

(i) If $0 < x < P_{O_2}$, then the radical reacts with O_2.
(ii) If $P_{O_2} < x < (P_{O_2} + P_{XSH})$, then the radical reacts with XSH.
(iii) If $(P_{O_2} + P_{XSH}) < x < (P_{O_2} + P_{XSH} + P_{RH})$, then the radical reacts with RH.
(iv) Otherwise, it may react with another species, depending on their distance and the respective reaction radius (Boscolo *et al* 2018).

3. Results

3.1. Code validation

3.1.1. Experimental data in water environment at extended time scales

This section presents a comparative analysis between two experimental findings, derived under neutral pH conditions from the data of Roth and LaVerne (2011), and TRAX-CHEMxt predictions. The G-value of H_2O_2 is selected as the final endpoint, being a stable molecule within the considered framework (Shin *et al* 2024). Around $1\,Gy\,s^{-1}$ was delivered for both radiation qualities, ^{60}Co γ and proton, with doses of up to 1350 Gy for the former and 300 Gy for the latter. A time scale of 15 min is therefore deemed sufficient for saving the computational yields. Projectiles' energies are simulated, such that their respective track segment LETs (in cylindrical targets with heights $\approx 5\,\mu m$) correspond to the track average ones associated with the relative experimental beams. The uncertainties for the final computed values are derived from a quadratic summation between the ones related to the concentration distribution algorithm (σ_{xt})—supplementary material in Camazzola *et al* (2023), and the MC ones (σ_{MC})—standard error from all independent simulated tracks: $\sqrt{\sigma_{MC}^2 + \sigma_{xt}^2}$.

In the first experimental set-up (Roth and LaVerne 2011), a ^{60}Co γ source was employed for the irradiation of a fully aerated water environment. A 500 keV electron track in a target with $pO_2 = 19\%$ is simulated for the chemical yields comparison, due to the similar LET, $0.2\,keV\,\mu m^{-1}$ (Camazzola *et al* 2023). Figure 1 summarises both the radicals' and molecules' trends predicted by TRAX-CHEMxt, as well as the data from Roth and LaVerne. The final experimental yield is $G\text{-value}(H_2O_2)_{exp} = (0.96 \pm 0.05)$ molecules/100 eV, whereas $G\text{-value}(H_2O_2)_{theo} = (1.2 \pm 0.2)$ molecules/100 eV is the theoretical one. Differences might be due to the physical properties of the two radiation qualities. In fact, ^{60}Co γ is featured by an energy spectrum, with two energy lines at 1.17 MeV and 1.33 MeV. In general, the two values exhibit reasonable compatibility.

In the second experimental scenario (Roth and LaVerne 2011), a 5 MeV proton beam, with track average LET $= 20.7\,keV\,\mu m^{-1}$ (Pastina and LaVerne 1999), was employed. Since TRAX works in a track

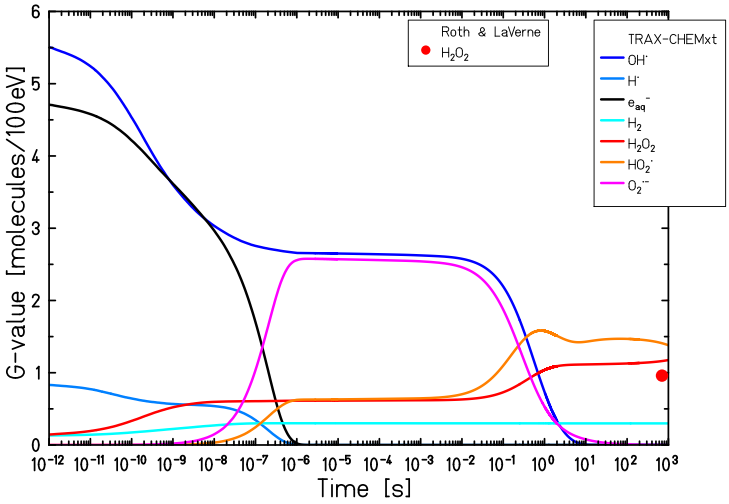

Figure 1. H_2O_2 yields comparison between the experimental data from Roth and LaVerne (Roth and LaVerne 2011), and the theoretical prediction from TRAX-CHEMxt. Whereas the former employed a ^{60}Co γ source, for the computation a 500 keV electron track in a water environment with $pO_2 = 19\%$ is simulated, due to their similar LET, around 0.2 keV μm^{-1}. The uncertainty of the experimental value is smaller than the symbol and therefore not visible.

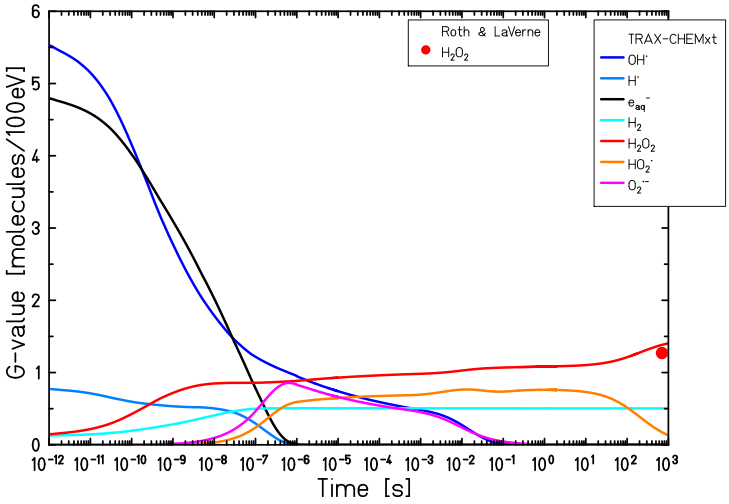

Figure 2. H_2O_2 yields comparison between the experimental data from Roth and LaVerne (2011), and the theoretical prediction from TRAX-CHEMxt. Whereas the former employed a 5 MeV proton beam, for the computation a 1.5 MeV proton track in a water environment with $pO_2 = 19\%$ is simulated, due to their similar LET, around 20 keV μm^{-1}. The uncertainty of the experimental value is smaller than the symbol and therefore not visible.

segment condition, to compare with this data, a 1.5 MeV monoenergetic proton track with a constant LET of 19.7 keV μm^{-1} is simulated, still in a fully aerated environment. The *G*-values are reported in figure 2. In this case the final yields are $G\text{-value}(H_2O_2)_{exp} = (1.27 \pm 0.07)$ molecules/100 eV for the experiment, and $G\text{-value}(H_2O_2)_{theo} = (1.40 \pm 0.04)$ molecules/100 eV for TRAX-CHEMxt. Also here, the two values exhibit a good agreement.

3.1.2. MC simulations in biological environment at overlapping time scales

The objective is now to demonstrate the reliability of TRAX-CHEMxt in conveying the information provided by the MC counterpart, in the context of a more complex environment. This is accomplished by monitoring the deviations between the two algorithms' predictions at an overlapping time scale. TRAX-CHEM outputs (both *G*-values and concentration distributions) recorded up to 10 μs and from different primary particle qualities, LETs, and O_2 levels, are compared with those obtained by the combination of TRAX-CHEM (up to 1 μs) and TRAX-CHEMxt. With respect to the previous analysis (Camazzola *et al* 2023), due to the change in the kinetics and to let the system achieve the local homogeneity within each bin of the concentration distributions, the information transition between TRAX-CHEM and TRAX-CHEMxt is set to 1 μs. The primary water radicals, i.e. $OH^{\bullet}$, e_{aq}^{-}, and $H^{\bullet}$, are not

Table 4. Maximum differences associated with TRAX-CHEMxt, for the four initial conditions simulated. Each deviation is derived by taking the biggest value from the absolute differences between the total number of every radical and molecule predicted by the extension (with initial concentrations taken from MC at 1 μs) and the respective quantities produced by TRAX-CHEM, divided by the latter.

Particle type	Energy	pO_2 (atm)	Max difference at 10 μs
Electrons	500 keV	0.5%	5%
Electrons	500 keV	21%	5%
Carbon ions	90 MeV u^{-1}	0.5%	3%
Carbon ions	90 MeV u^{-1}	21%	3%

shown, as they are all already fully consumed before the switching time. Also HO_2^-, R_2, and ROOR are not considered, due to their very low yields.

A 500 keV electron track and a 90 MeV u^{-1} carbon track are examined, irradiating a target at two extreme oxygenation levels, 0.5% and 21%. All final *G*-values show differences below 5% with respect to the MC counterparts, as documented in table 4. In figure 3, examples of TRAX-CHEMxt concentration distributions, saved at 5 μs and 10 μs, are compared with the respective TRAX-CHEM ones. Good agreements are registered for all chemical species and all initial conditions investigated. Overall, a preserved level of accuracy by TRAX-CHEMxt is evident.

3.1.3. Experimental data in biological environment at extended time scales

A final benchmark is performed by comparing TRAX-CHEMxt predictions with the experimental data from Karle *et al* (2024), in the context of radiolytic oxygen depletion (ROD) within a biological target. Different conventional radiation types are selected for testing, i.e. proton, helium, carbon, and oxygen ions. Their simulation energies are retrieved using the same approach proposed in section 3.1.1 to match the reported LETs, so respectively 8 MeV ($\approx$5.1 keV μm^{-1}), 11 MeV u^{-1} ($\approx$14.9 keV μm^{-1}), 25 MeV u^{-1} ($\approx$66.5 keV μm^{-1}), and 30 MeV u^{-1} ($\approx$101 keV μm^{-1}). The simulated biological system is implemented to mimic the experimental condition, meaning that the RH molecule stands now for the bovine serum albumin (BSA), and is present at a concentration of 5% (or 750 μM). On the other hand, XSH is set to 0 μM as no enzymes are considered. Following the same logic, new reaction rate constants are introduced as well, and listed in table 5. The diffusion coefficient assigned to BSA and its radical is derived from Gaigalas *et al* (1992), and amounts to $6 \cdot 10^{-11}$ m^2 s^{-1}. All radiation qualities are tested for a set of 8 different oxygenation levels: (0.1%, 0.2%, 0.3%, 0.5%, 0.8%, 2%, 5%, 13%). Figure 4 summarises both the theoretical and experimental ROD.

As a general trend, the oxygen depletion values decrease with increasing particle LET. Similarly, the fluctuations between the experimental data points reduce as well. TRAX-CHEMxt's outputs have been recorded up to 1 s post irradiation, in accordance with the time resolution of the OxyLite system used (Karle *et al* 2024). The ROD values in the saturation regions seem to be reproduced fairly acceptably by simulations, showing also a lowering tendency when passing from low to high LETs. However, a very steep increase under low oxygenations is registered, while the data from Karle and co-authors show a slower 'shoulder' formation with increasing initial oxygen level. Some possible reasons for the discrepancy are proposed in section 4.1.

3.2. Medium impact on chemical yields

The *G*-values produced in different environmental conditions by two radiation qualities, 500 keV electrons and 90 MeV u^{-1} carbon ions, are compared. The data on H_3O^+, OH^-, and H_2 are not shown, as their yields depend on the stoichiometric decisions made to conserve the reactants' masses (i.e. to preserve the amount of each element in both reactants and products, cf the two sides of the 'Reaction' column in table 2). Also the yields of HO_2^-, R_2, and ROOR are not reported, due to their low amounts. Conversely, both $XS^\bullet$ and $HS^-/X^\bullet$ are still considered to be of value, since they provide useful information on the actual amount of XSH that 'intervened' within the chemical network. The *G*-values for HS^- and $X^\bullet$ have been depicted with the same colour, because they are produced always in the same amount as evidenced by reaction (xxxvi) in table 2.

Figures 5 and 6 report the primary chemical yields produced up to 1 s under pO_2 of 0.5% and 21%, for both a water and a biological environment. The following considerations can be applied to both radiation qualities simulated. As far as the H_2O target is concerned, the primary radicals are completely consumed at (1–10) μs for $H^\bullet$ and e_{aq}^-, reaching (0.1$-$ $>$1) s for $OH^\bullet$. The respective products, H_2 and H_2O_2, exhibit a constant increase. Concomitantly, the oxygen present in the target starts to play a prominent role in the network at approximately 1 μs for 0.5% pO_2, shortening to 10 ns for 21% pO_2, as both

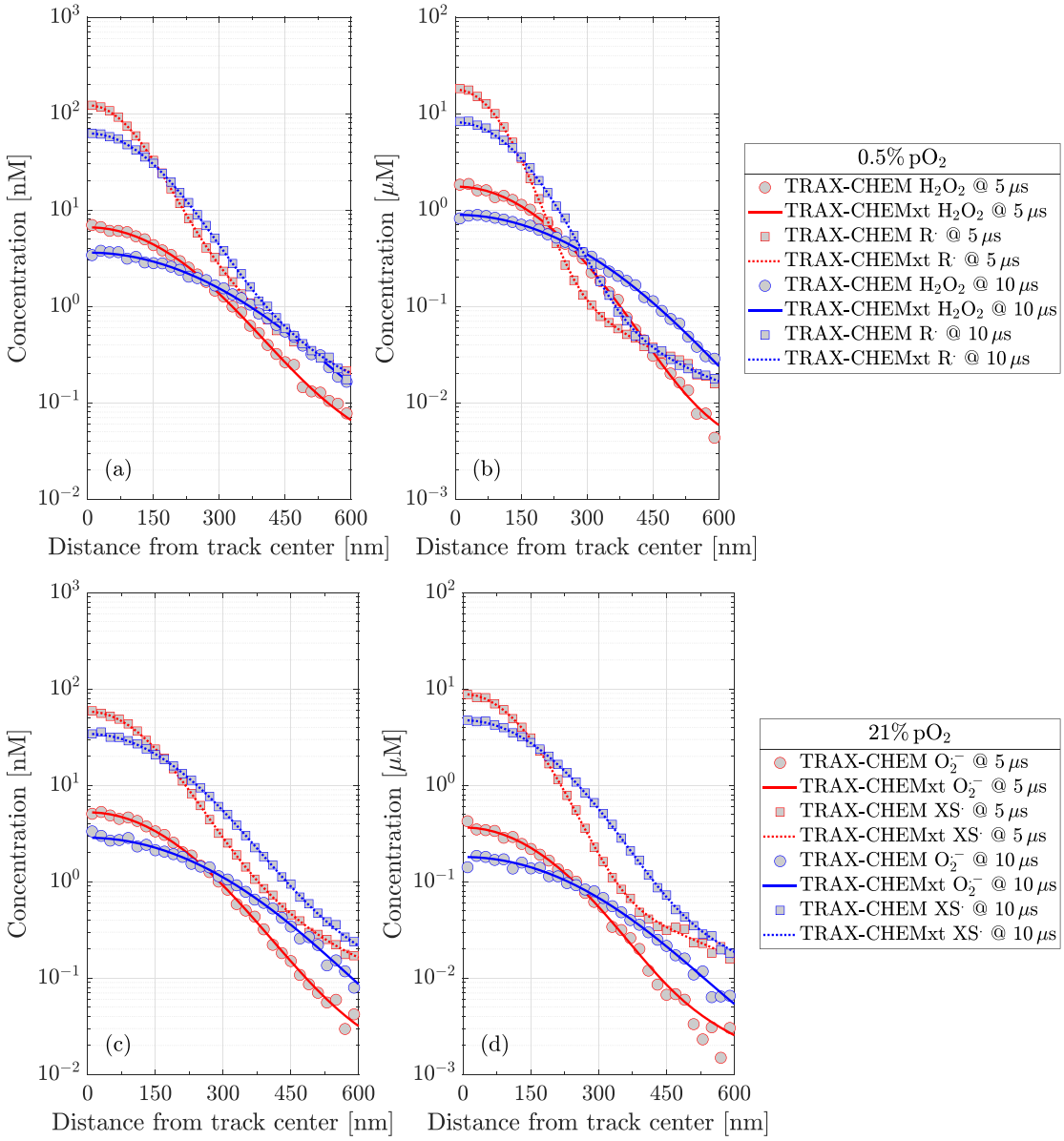

Figure 3. Examples of compared radial concentration distributions for H_2O_2, $R^\bullet$, $O_2^{\bullet-}$, and $XS^\bullet$, produced by a 500 keV electron track (a), (c) and a 90 MeV u^{-1} carbon track (b), (d), under oxygenations of, respectively, 0.5% (a), (b) and 21% (c), (d).

Table 5. List of reactions and respective reaction rate constants assumed for the comparison with the experimental data in Karle *et al* (2024). In this context, RH stands for BSA (750 μM), while no XSH is included.

	Reaction	κ [10^{10} dm^3 mol^{-1} s^{-1}]	References
(i)	$OH^\bullet + RH \rightarrow R^\bullet + H_2O$	3	Adhikari and Gopinathan (1996)
(ii)	$e_{aq}^- + RH + H_2O \rightarrow H_2 + R^\bullet + OH^-$	1	Schuessler and Davies (1983)
(iii)	$R^\bullet + O_2 \rightarrow ROO^\bullet$	0.01	El Khatib *et al* (2022)
(iv)	$R^\bullet + R^\bullet \rightarrow R_2$	0.01	Labarbe *et al* (2020)

$HO_2^\bullet$ and $O_2^{\bullet-}$ are produced in a considerable increasing amount. Some long-lasting reactions at times >1 ms can be spotted as well, for both oxygenations, mostly consuming the hydroxyl radicals ($OH^\bullet$) and superoxide anions ($O_2^{\bullet-}$), producing further H_2O_2 and $HO_2^\bullet$. The situation changes drastically when dealing with the biological milieu. All primary water radicals are fully consumed already around 100 ns, due mostly to reactions with both RH and XSH at times as small as 1 ns. To correctly describe these reaction network dynamics, the biomolecules have to be included within the MC algorithm, for both particle tracks. Some species such as H_2O_2, $HO_2^\bullet$, and $O_2^{\bullet-}$, are produced in lower yields with respect to the oxygenated H_2O targets, due to the scavenging of primary water radicals. Concurrently, the increase of the biological radicals, $R^\bullet$, $XS^\bullet$ and $HS^-/X^\bullet$, is evident. A slightly lower $R^\bullet$ peak is registered for the

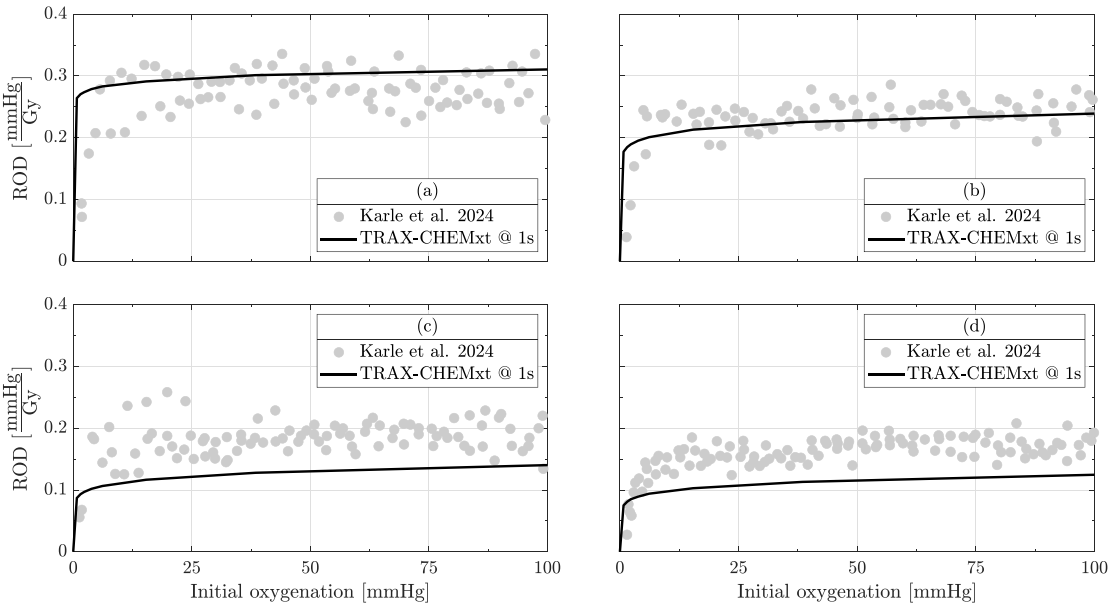

Figure 4. Radiolytic oxygen depletion values predicted by TRAX-CHEMxt and reported in Karle *et al* (2024), for respectively 8 MeV protons (a), 11 MeV u^{-1} helium ions (b), 25 MeV u^{-1} carbon ions (c), and 30 MeV u^{-1} oxygen ions (d).

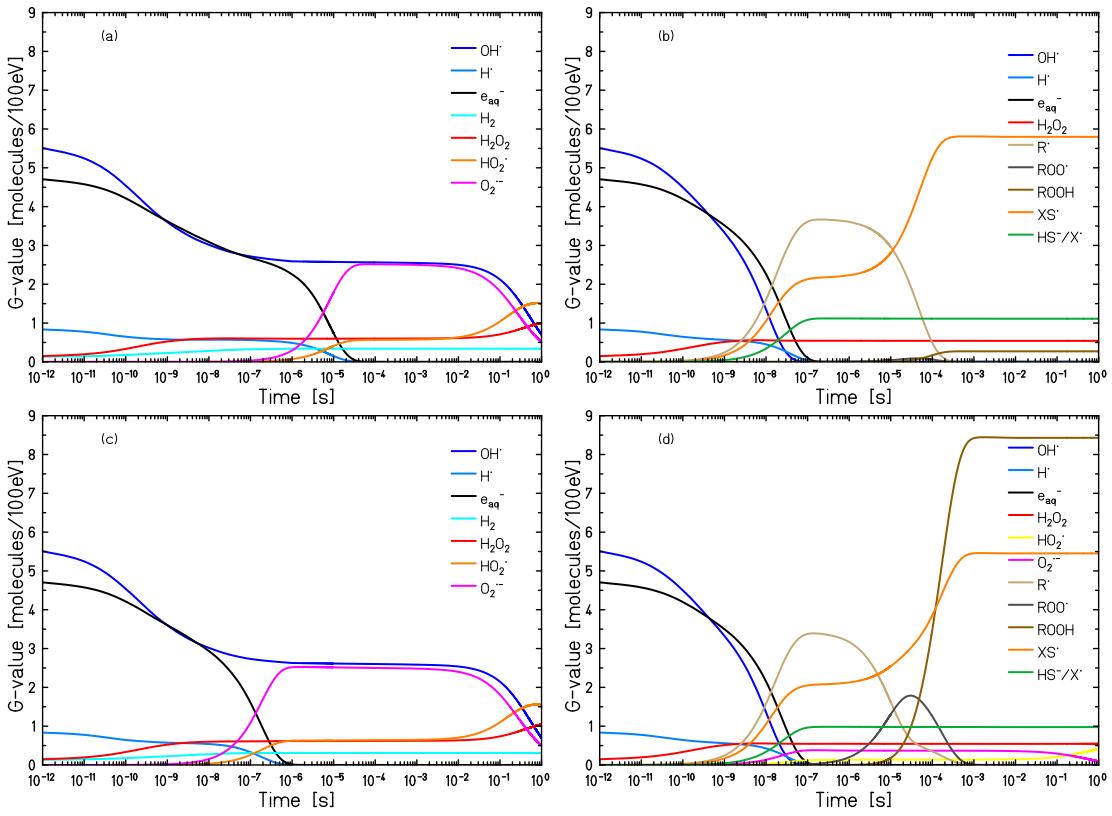

Figure 5. *G*-value curves for the major species produced by a 500 keV electron track in a water (a), (c) and biological (b), (d) environment, with $pO_2 = 0.5\%$ (a), (b) and 21% (c), (d), recorded up to 1 s.

21% pO_2 case with respect to 0.5%, because some $H^{\bullet}/e_{aq}^{-}$ are converted into $HO_2^{\bullet}/O_2^{\bullet-}$, respectively. Similarly, also the $HS^{-}/X^{\bullet}$ yields are a bit smaller at full oxygenation. A higher final $XS^{\bullet}$ *G*-value is registered for the hypoxic condition, meaning that here XSH interacts mostly with $R^{\bullet}$. Vice versa, at full oxygenation, the fixation reaction between $R^{\bullet}$ and O_2 prevails. The $ROO^{\bullet}$ level increases, with a production that starts before 1 μs for the environment at 21%. Additionally, the $R^{\bullet}$ curve 'slows down' its decreasing slope, around 30 μs. This behaviour is due to the chain propagation reaction reported in (4),

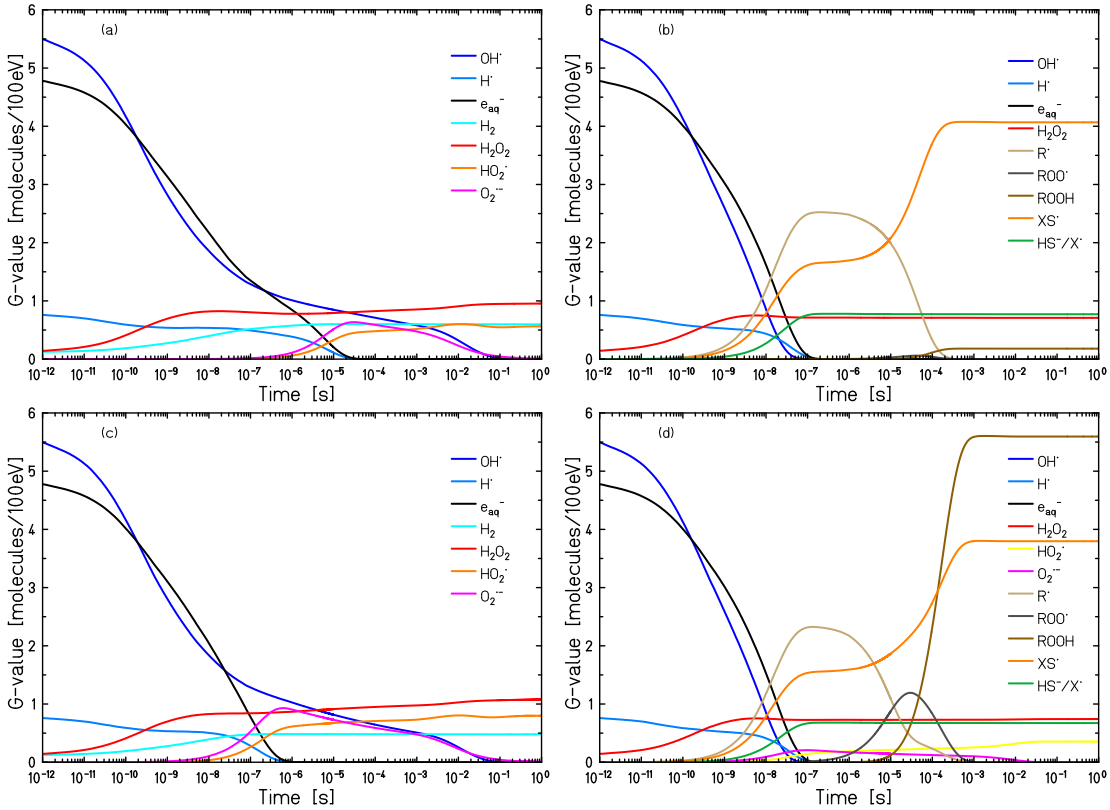

Figure 6. *G*-value curves for the major species produced by a 90 MeV u^{-1} carbon track in a water (a), (c) and biological (b), (d) environment, with $pO_2 = 0.5\%$ (a), (b) and 21% (c), (d), recorded up to 1 s.

where the organic peroxyl radicals and other RH molecules react, not only producing hydroperoxides, but reintroducing in the system new $R^{\bullet}$ as well. In this situation, the intervention of XSH would be mostly against $ROO^{\bullet}$, to terminate the chain propagation. A clear indication of these chemical interactions is the great increase in the 'damaged' end-product ROOH. In section 3.3, an analysis is carried out to understand the dependence of this yield on LET, whereas in section 4.2, the reason behind this rise is investigated. With respect to the water milieu, the O_2 impact is shifted to later times, and the effects of the aforementioned reactions prove the necessity to simulate longer time scales. The introduction of the biological species has therefore impacted significantly the species yields (Shin *et al* 2024, D-Kondo *et al* 2025).

3.3. Organic hydroperoxide dependence on LET

The organic peroxyl radical $ROO^{\bullet}$ is a non-restorable form of the target RH, resulting from the damage fixation performed by oxygen (Favaudon *et al* 2022). Its amount can therefore be treated as an indicator of the indirect damage, as proposed by Thomas *et al* (2024). Consequently, the yield of ROOH has to be monitored (El Khatib *et al* 2022), representing the final stable altered biomolecule (Liu and Gebicki 2012). This section is dedicated to the investigation of the influence of LET on the ultimate yield of organic hydroperoxide. A biological environment under different oxygenation conditions, respectively 1%, 4%, 7%, and 15% pO_2, is simulated. Table 6 summarises all the LET considered, together with the related particle types and energies. The data are saved at 1 ms, to ensure that the saturation of ROOH is reached in the various scenarios. The resulting *G*-values are summarised in figure 7.

The competition between oxygen fixation and intratrack recombination effects is evident. After the delivery of low LET radiations, water radicals are distributed far apart, favouring reactions with the environment—first with RH and XSH, later with O_2, due to their different concentrations. This leads to the subsequent chain cascade, reactions (xxviii) and (xxxi) in table 2. Final values of (0.54 ± 0.02) molecules/100 eV, (2.06 ± 0.01) molecules/100 eV, (3.43 ± 0.01) molecules/100 eV, and (6.53 ± 0.02) molecules/100 eV, for increasing pO_2, are registered. As the LET rises, so do the radical recombination rates, due to the enhanced proximity between the chemical species. Consequently, the amount of radicals available for reacting with the biomolecules is reduced, limiting the final ROOH formation. In all oxygenation conditions, it is decreased by roughly 70%. These results corroborate the

Table 6. Particle qualities and respective energy and LET values used in the simulations.

Particle type	Energy	LET (keV μm^{-1})
Electrons	500 keV	0.2
Protons	65 MeV	1
Helium ions	150 MeV u^{-1}	2
Helium ions	50 MeV u^{-1}	5
Carbon ions	300 MeV u^{-1}	10
Carbon ions	150 MeV u^{-1}	20
Carbon ions	40 MeV u^{-1}	50
Carbon ions	20 MeV u^{-1}	90
Oxygen ions	16 MeV u^{-1}	200
Neon ions	17 MeV u^{-1}	300

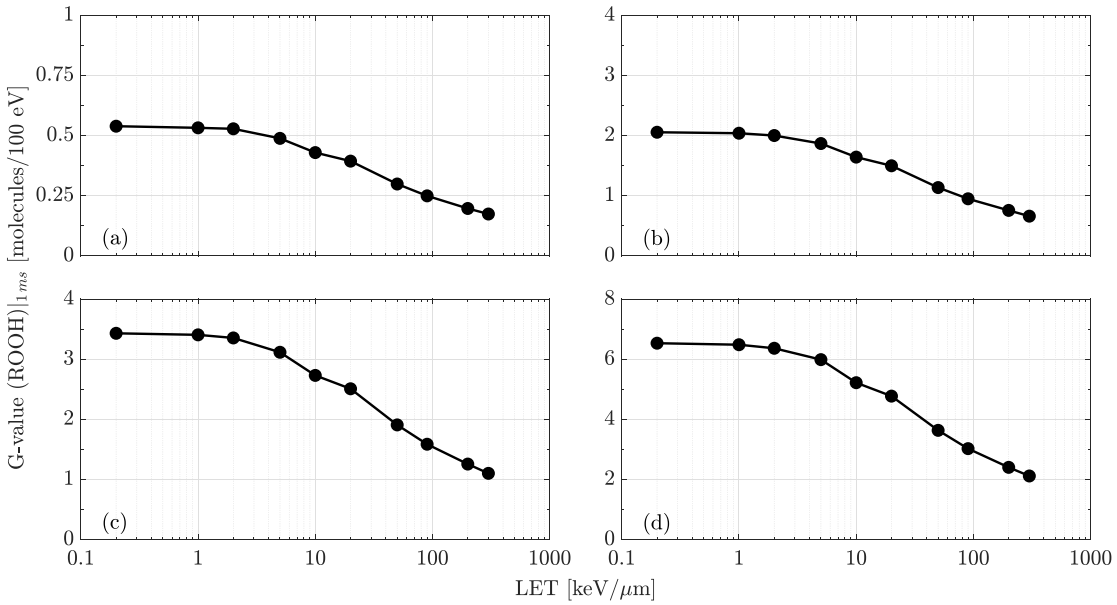

Figure 7. *G*-values of the organic hydroperoxide ROOH as a function of LET. The environment simulated is kept at a constant oxygen level of 1% (a), 4% (b), 7% (c), and 15% (d). The data are recorded at 1 ms.

assertion that there are significant differences in the proportion of indirect damage with respect to the primary radiation quality under consideration. To monitor the oxygen effect in the ROOH yield, the ratios of the *G*-values at various oxic conditions to the one in hypoxia are computed. The outcomes are shown in figure 8.

An increase in the oxygenation from 1% to 4%, 7%, and 15% induces a rise in the ROOH yield of around 3.5 fold, 6 fold, and 12 fold respectively, regardless of the LET simulated. Consequently, within this pO_2 domain, different levels of oxygen—ubiquitous in the target—simply anticipate/delay (time-wise) the reactions with the $R^{\bullet}$ radicals, but do not unlock other new channels.

4. Discussion

4.1. Code validation

With the new environment implemented both in TRAX-CHEM and TRAX-CHEMxt, it has been possible to investigate the chemical effects of radiation in a biological target, probing on top longer time scales. To ascertain whether TRAX-CHEMxt provides reliable outcomes, its predictions have to be benchmarked first with experimental findings. This, however, represents a challenge (D-Kondo *et al* 2025). On the one hand, TRAX-CHEMxt is featured by inherent limitations associated with initial conditions that can be currently simulated, such as treatment of low dose rates and constant LETs. On the other hand,

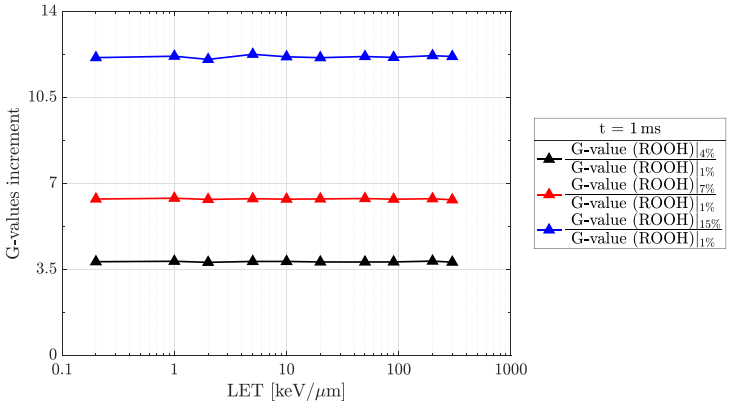

Figure 8. Increment in the *G*-values for the organic hydroperoxide ROOH as a function of LET, when passing from 1% to, respectively, 4%, 7%, and 15% pO_2. The data are recorded at 1 ms.

the amount of experimental data pertaining to chemical yields produced by ionising radiations at long temporal domains, even in a simple water target, is modest.

Literature data from Roth and LaVerne (2011) have been used as a benchmark for the theoretical predictions within an oxygenated water target. The final H_2O_2 yields reported, after the delivery of ^{60}Co γ and protons beams, were (0.96 ± 0.05) molecules/100 eV for the former, and (1.27 ± 0.07) molecules/100 eV for the latter. These, together with the theoretical calculations—final outcomes of respectively (1.2 ± 0.2) molecules/100 eV and (1.40 ± 0.04) molecules/100 eV, were documented in figures 1 and 2. Overestimations from TRAX-CHEMxt appeared. One reason can be referred to the approximation used regarding the track segment LETs chosen. Taking the proton case as an example, for achieving the same LET, around 20 keV μm^{-1}, as that reported in the experiment (i.e. under track average conditions, with a beam of 5 MeV), the energy assigned to the projectile simulated in a track segment set-up was 1.5 MeV. This means that, while from the simulation a 1:1 relation between the proton energy and the H_2O_2 amount can be established, the final yield from the experiment is related to the total energy deposited by the primary beam, from 5 MeV until it stops. Consequently, in this latter scenario there will invariably be a greater contribution from lower LET components with respect to the track segment one, as the energy domain (1.5–5) MeV is larger than the (0–1.5) MeV one, resulting in a net reduction of the molecular yields. An additional cause of discrepancy can be the reaction scheme implemented, since low rate coefficients featuring specific channels are disregarded in the one currently used in TRAX-CHEMxt. As postulated by Pastina and LaVerne (2001), Roth and LaVerne (2011), 'higher-order' reactions, characterised by relatively low values of κ, may become relevant at longer time scales. Finally, the acid-base equilibrium has to be addressed. Within the experimental environment, the pH was neutral, and since the acid dissociation constant for the pair $HO_2^\bullet / O_2^{\bullet -}$ is 4.9 (Labarbe *et al* 2020), some of the hydroperoxyl radicals actually convert into their respective conjugated base. This mechanic is not yet implemented in TRAX-CHEMxt, therefore an overestimation of $HO_2^\bullet$ is expected, with a consequently larger production of hydrogen peroxide via $HO_2^\bullet + HO_2^\bullet \rightarrow H_2O_2 + O_2$. Overall, the results are satisfactory, emphasising the significance of higher-order reactions on the final products yields due both to species spatial distributions and their concentration values.

A well-constructed computational model can facilitate the distinction between disparate primary projectile qualities, from a physical and chemical standpoint. This is an important characteristic that has been highlighted by Favaudon *et al* (2022), Thomas *et al* (2024). The implementation of new species in the reaction network, RH and XSH (tables 1–3), enabled a radiation chemistry analysis in a target which was more complex than simple oxygenated water. The objective was to examine species that are ubiquitous within the cell, so no specific biomolecules were targeted (e.g. a specific protein type). Similarly, also the attack on DNA was not considered. This is due to the fact that DNA is highly site-specific, necessitating the division of the implemented environment into a 'nucleus' and a 'cytosol', with lipid membranes in between. The actual simulation of this conformation is a highly complex undertaking, and the crucial approximation of concentration distributions would have been challenged around the lipid bilayers, necessitating a different approach for computing radicals' diffusion. Since this was a preliminary study on the effects of new species in a water target, the dynamics' parameters were deemed suitable for

the analysis, given that the precise nature of the biomolecules was not a primary concern. In fact, rate constants for, e.g. dimerisation processes like $R^{\bullet} + R^{\bullet} \rightarrow R_2$, are very molecule-dependent (Hawkins and Davies 2001, Shin *et al* 2024). It is therefore complicated to determine a representative value for κ.

Still from the validation standpoint, outcomes from TRAX-CHEM and TRAX-CHEMxt in the overlapping time frame, (1–10) μs, were compared. Good agreements were found for both concentration distributions, figure 3, and *G*-values, table 4, regardless of the initial conditions considered or the specific chemical species under investigation. Only in cases of particularly low yields (<0.1 molecules/100 eV) uncertainties arose. Two main reasons can be discerned. First, TRAX-CHEM is capable of tracking chemical species that exit the volume of interest, both laterally and longitudinally. However, in the current implementation, there is no 'equilibrium' at the borders of the target. This means, from the chemical point of view, that the species going out are not balanced by others coming in. The track density (concentration distributions) and the related reactions will be different depending on whether a balance is maintained or not, mostly along the longitudinal direction of the primary ion. It is clear that a species has a higher chance of reacting with others produced by the track if it is kept within the target (ricochet at the boundaries), rather than if it is let go outside of it, due to different local densities encountered. As a consequence of the approximation employed in TRAX-CHEMxt, the balance of species along the longitudinal and radial directions is always maintained. This difference became effectively evident only when dealing with very low numbers, as for instance R_2 and ROOR, which are featured by yields representing less than one actual radical/molecule, having practically no meaning. The yields related to the most important final species, ROOH, that actually derives from a series of reactions ($R^{\bullet} \rightarrow ROO^{\bullet} \rightarrow ROOH$) always resemble the MC ones, with deviations <3%. A second reason can be due to differences in the resolution of the reactions between the two algorithms. In the MC case, the reaction radii act as a limiting factor. Once a species has reacted, it is removed from the milieu. Conversely, this sort of binary behaviour is not present when a concentration representation is considered. Minor discrepancies may then arise between the 'quantised' approach of TRAX-CHEM (step-by-step), and the 'continuous' concentration distributions approach of TRAX-CHEMxt (1D conversion). Small deviations aside, keeping monitored the track structure dependence enabled the formulation of a reliable and comprehensive description of the chemical dynamics, encompassing a wide range of radiation and environmental conditions.

A further set of experimental data, from Karle *et al* (2024), was considered for benchmarking the simulations, this time within a biological milieu. The reaction system was modified to account for the presence of BSA, with new reaction rate coefficients reported in table 5. In figure 4, the ROD values along the four plateau fall within the range of the experimental data, showing an overall decrease while increasing the projectile LET. The discrepancies observed in the carbon and oxygen cases can be attributed to the approximation employed to simulate the respective tracks. Indeed, the experiment reported mean dose-averaged LETs of 65 keV μm^{-1} and 100.3 keV μm^{-1}, respectively, with actual ranges of (56–153) keV μm^{-1} and (88–235) keV μm^{-1}, whereas the simulated (instantaneous) track segment ones were found to be 66.5 keV μm^{-1} and 101 keV μm^{-1}. Additional secondary reaction channels that have not been included in the present simulations might also contribute to the different outcomes. Conversely, the theoretical RODs at low oxygenations overestimated the experimental ones. One observation that emerged during the course of the simulations was that the final recording time had a decisive impact on the formation of the shoulder. No explicit time was documented, however, 1 s was deemed sufficient, due to the resolution of the OxyLite system utilised. In this regard, a comparison between the outputs of instruments with different time resolutions would be interesting, to provide valuable insight into whether this final time can be reduced. It is also conceivable that the reaction scheme currently employed was not complete, potentially lacking some secondary reactions that could play a significant role under low oxygenation conditions. Although there is room for improvement, this evaluation demonstrated a positive aspect of algorithm, namely its capacity to emulate diverse biological environments.

4.2. Medium impact on chemical yields

In figures 5 and 6, a comparison between the yields produced under different oxygenations and environmental conditions, by a 500 keV electron and a 90 MeV u^{-1} carbon ion tracks, was carried out. For the pure water target, the chemical species behaved as expected: radicals were consumed, and the respective products were generated. Also $HO_2^{\bullet}$ and $O_2^{\bullet -}$ were formed, once the species distributions were more diffused and could be affected by O_2. Some long-lasting reactions (millisecond to second frame) were present as well, with a temporary equilibrium recorded for H_2O_2 and $HO_2^{\bullet}$ at 1 s. Hydroperoxyl radicals recombinations are expected at later times. As far as the biological milieu is concerned, incorporating both RH and XSH components already in the MC stage was crucial, since all primary water radicals

were consumed in less than 1 μs, as observed in Liu and Gebicki (2012). The system dynamics can be divided into three principal and partially overlapping temporal domains. The initial one, spanning from 1 ps to 100 ns, is characterised by reactions involving $OH^{\bullet}$, $H^{\bullet}$ and e^{-}_{aq}, which predominantly interact with the biological environment. Some products that will remain stable are formed, namely H_2O_2 and $HS^{-}/X^{\bullet}$. During the second time domain, from 1 ns to 1 ms, the chemical network is dominated by the biological radicals, which exert a major influence on the reaction events. $R^{\bullet}$ reached a maximum of approximately 3.5 molecules/100 eV if stemming from the electron track, and 2.5 molecules/100 eV if from the carbon ion, at 100 ns. It will subsequently decrease due to the presence of oxygen, whose effect started to be discernible after 1 μs (Spitz *et al* 2019, Cao *et al* 2021, Favaudon *et al* 2022). A delay in the formation of $ROO^{\bullet}$ was observed, likely attributable to competing reactions with antioxidants (Liu and Gebicki 2012). Although a considerable amount of XSH intervened already at the ns time scale, the majority reacted with $R^{\bullet}$ at later times, between tens and hundreds of μs. During this final time domain, 10 μs to 1 s, a significant increase in reaction activity was observed for all scavengers. Under full oxygenation, the final amount of ROOH was greater than the initial yields of primary water radicals, suggesting a decisive contribution stemming from oxidation events occurring within chain reactions (Liu and Gebicki 2012).

To clarify why ROOH increases so much, the focus should be given to the specific network implemented, and more in detail to the reactions featuring the three scavengers at times longer than the μs, deemed to be responsible for the aforementioned outcome. In other terms, the competition between $R^{\bullet} + O_2$ (fixation) and $R^{\bullet} + XSH$ (neutralisation), and between $ROO^{\bullet} + RH$ (chain propagation) and $ROO^{\bullet} + XSH$ (chain termination)

$$\begin{cases} R^{\bullet} + O_2 \rightarrow ROO^{\bullet} & \kappa = 2.3 \cdot 10^{8}\,\mathrm{dm^3 mol^{-1} s^{-1}} \\ ROO^{\bullet} + RH \rightarrow ROOH + R^{\bullet} & \kappa = 5 \cdot 10^{5}\,\mathrm{dm^3 mol^{-1} s^{-1}} \\ R^{\bullet} + XSH \rightarrow RH + XS^{\bullet} & \kappa = 5 \cdot 10^{6}\,\mathrm{dm^3 mol^{-1} s^{-1}} \\ ROO^{\bullet} + XSH \rightarrow ROOH + XS^{\bullet} & \kappa = 5 \cdot 10^{5}\,\mathrm{dm^3 mol^{-1} s^{-1}} \end{cases} \quad (6)$$

have to be studied. The first two events in (6), taken from table 2, enable the continuation of the reaction activity, whereas in the latter ones, the antioxidant intervenes to decelerate it. TRAX-CHEMxt can save the contributions of the various reactions within one simulation loop, and figure 9 shows examples of these contributions. Both major and minor channels featuring the biomolecules are considered, comparing as well the cumulative final effects on the various species produced by a 90 MeV u^{-1} carbon ion track in an environment with a 21% pO_2. Because the concentrations which define the reactions depend on the selected bin and change over time due to the effects of diffusion, absolute values are not meaningful. The data reported, for simplicity, relates to the first bins of each distribution. The minor channels contribute to their respective species at least three orders of magnitude less than the major ones. They are only presented for the sake of completeness. Referring to panel (d) in figure 6, two time frames are chosen: one around the $ROO^{\bullet}$ peak, $\approx$30 μs, the other when $R^{\bullet}$ and $ROO^{\bullet}$ are converging to zero, $\approx$300 μs. The contributions stemming from the various reactions are almost constant as time proceeds, with only an overall decrease in absolute magnitude, due to a lower amount of active radicals, and a reduced oxygen intervention at longer temporal scales.

At 30 μs, oxygen depletion due to $R^{\bullet}$ is the most significant reaction with respect to all the others in the system. The high O_2 consumption is explained by the fact that $R^{\bullet}$ and $ROO^{\bullet}$ register a very slow decrease. As a consequence of chain reactions, the net impact on the radicals depletion is diminished, with around 70% to 90% of the reacted species that are reintroduced in the milieu. The new $R^{\bullet}$, in turn, have high chances to consume other O_2. Only at later times, after 1 ms, both $R^{\bullet}$ and $ROO^{\bullet}$ are entirely consumed. Consequently, the yield of ROOH increases rapidly, with the primary contribution arising from the loop reaction with the substrate RH. Although having the same rate coefficient as the reaction with the antioxidant, the concentration of RH is one order of magnitude larger than that of XSH (table 1). This results in a contribution to the total ROOH yield of approximately 90% from $ROO^{\bullet} + RH$, with the remaining 10% derived from $ROO^{\bullet} + XSH$.

4.3. Organic hydroperoxide dependence on LET

An investigation was also conducted to examine the impact of LET on the final ROOH yield, representing the stable end product stemming from the non-restorable form of the original target RH, i.e. $ROO^{\bullet}$. An inverse relation was found for all four oxygenation levels tested, figure 7, representing the competition between oxygen fixation and radicals (intratrack) recombination. Under low LETs, reactions with the milieu occurred with a higher frequency, due to the broader distribution of the radicals. For denser energy depositions, recombination events between the chemical species dominated the system

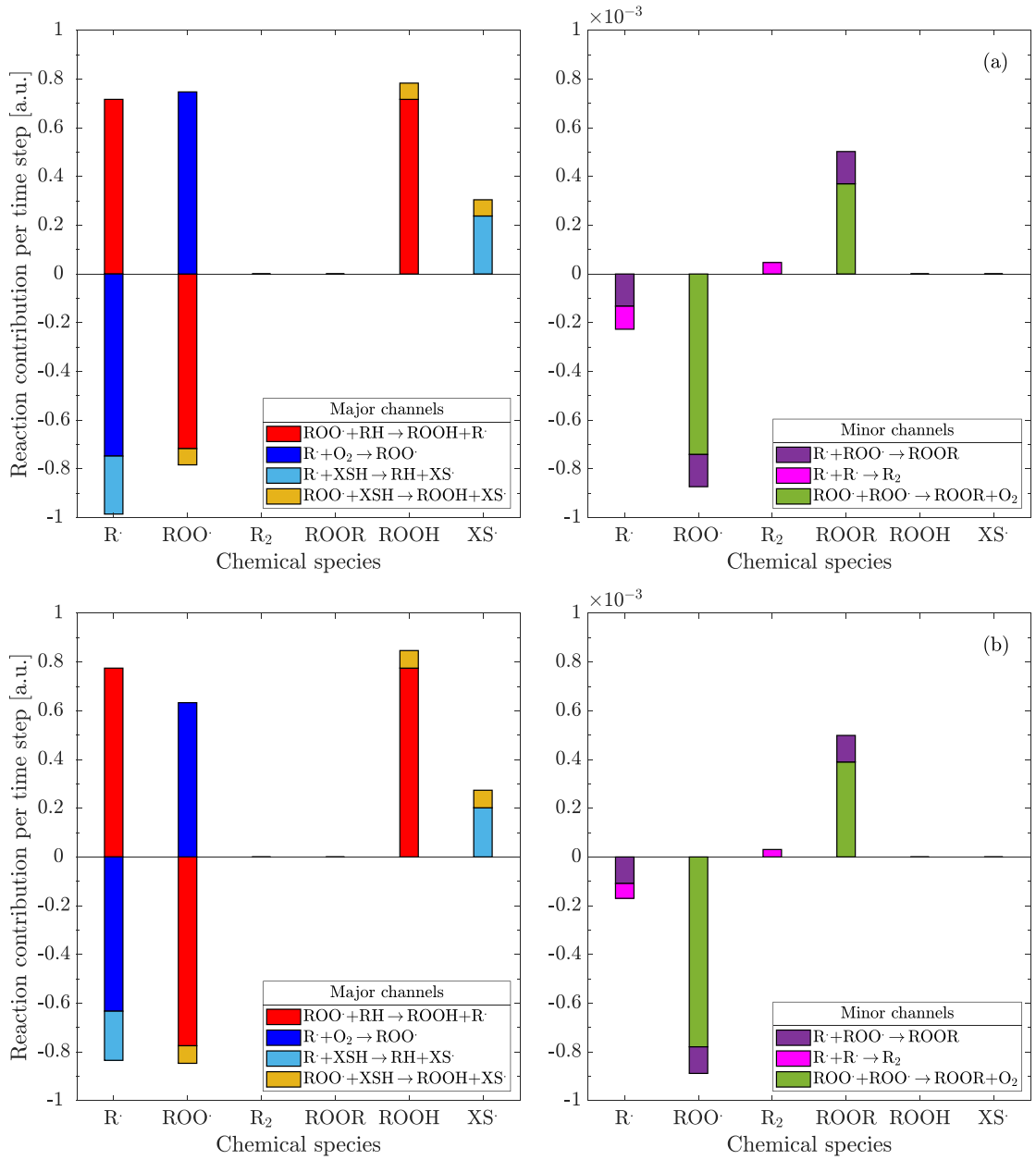

Figure 9. Reactions contributions (positive/production upwards and negative/reduction downwards) affecting the major biological species generated by a 90 MeV u^{-1} carbon track released in a biological environment with $pO_2 = 21\%$. They are saved at 30 μs (a) and at 300 μs (b). The results are obtained from the contributions associated to the first bin of the various concentration distributions. The minor channels contribute at least three orders of magnitude less to the respective species count than the major ones.

dynamics, resulting in lower interactions with RH. The slopes of the curves underwent indeed a change at approximately 2 keV μm^{-1}, transitioning from a constant amount to a linear decrease. This resulted in *G*-values of the organic hydroperoxide for the largest LET simulated, 300 keV μm^{-1}, around 70% lower with respect to the ones observed at low LETs. The indirect damage therefore changes considerably with respect to the radiation considered. An increase in the target oxygenation, from 1% to 4%, 7% and 15%, resulted just in a change of the final ROOH yield, by a constant factor of respectively 3.5, 6, and 12, regardless of the LET (figure 8).

During the analysis, it was observed that the ROOH yield exhibited a correlation with the reaction rate constant attributed to the oxygen depletion by $R^{\bullet}$—reaction (xxviii) in table 2. A further study was thus conducted to ascertain the sensitivity of the *G*-value(ROOH) to different κ values. As demonstrated in figure 10 for the lowest LET simulated, 0.2 keV μm^{-1}, the organic hydroperoxide yield at physiological oxygenation conditions (4% pO_2) is significantly influenced by the reaction rate constant. It can thus be concluded that for particular reactions, as $R^{\bullet} + O_2 \rightarrow ROO^{\bullet}$, precise κ values are imperative to replicate the observed phenomena under experimental conditions.

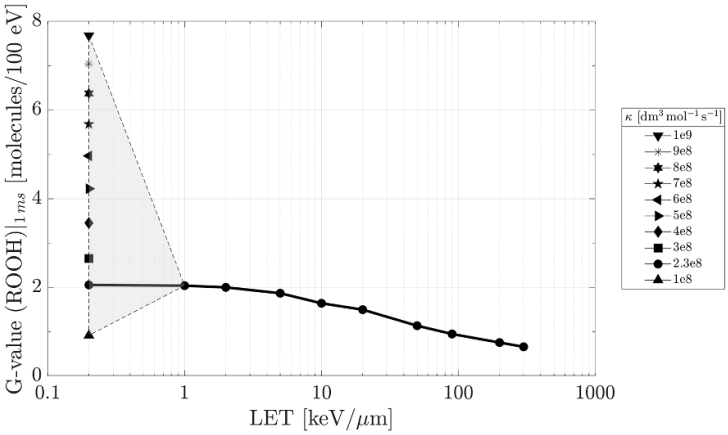

Figure 10. Variations in the ROOH *G*-value as a function of κ for the lowest LET simulated in figure 7, 0.2 keV μm^{-1}. The environment is kept at a constant oxygen level of 4%, and the data are recorded at 1 ms.

4.4. Final remarks

It is crucial to reiterate that all the findings in this work are exclusively associated with the simulated (generalised) environment, encompassing (for the chemical species considered) concentration values, reaction rate constants, and diffusion coefficients. Aside from the sensitivity analysis proposed in figure 10, two additional studies were carried out to evaluate the effects of variations in both concentration values and diffusion coefficients on the final molecular yields. The outcomes can be found in the Supplementary Materials of this work.

TRAX-CHEMxt limits to a few reactions and classes of biochemical species, and does not discriminate between them (proteins, amino acids and nucleotides, or GSH and $AscH^-$). In reality, the radicals can have different degrees of affinity with each specific substrate, resulting in possible variations in the final chemical yields, as pointed out by Favaudon *et al* (2022), Koch *et al* (2023). To achieve an optimal analysis of the indirect damage via the exploration of the biochemical stage, some possible future improvements can be made. Additional reactions can be contemplated, to observe potential effects of higher-order kinetics at the (μs–s) time scale. Within the context of an oxygenated water environment, noteworthy are the reaction schemes proposed by Pastina and LaVerne (2001) and Elliot and McCracken (1990), where more than 70 different reactions are reported, together with data on acid-base equilibria. Moreover, the actual separation of the various biological components can be performed, regarding both RH and XSH, in order to gain a more detailed understanding of the primary pathways involved in the induction and neutralisation of the damage. Ascorbate, as an example, demonstrated to be more effective than glutathione in restoring protein radicals back to RH (Liu and Gebicki 2012). The discrimination of different concentration values and reaction channels for antioxidants could also assist in distinguishing the effects between healthy and tumour environments, due to their differing abilities in restoring $R^\bullet$ to its unaltered state (Favaudon *et al* 2022). As reported in Koch *et al* (2023), the rates of antioxidant intervention change as a function of the substrates under consideration. More specific reactions can be included as well (Winterbourn 2016). In fact, within living cells, XSH is capable of undergoing a switching state process. This phenomenon occurs when a molecule reacted, prompting the activation of another one via signalling events, effectively 'filling the gap' and thereby maintaining its equilibrium. Taking for instance glutathione, its amount is 'restored' by a new synthesis or by the reduction of glutathione disulfide (GSSG) (Liu and Gebicki 2012). Furthermore, other species can be introduced in the system. Candidates are SOD, CAT, vitamin E as antioxidants, with also $CO_3^{\bullet-}$—which is shown to play an important role in DNA damage without irradiation (Fleming and Burrows 2020), $NO^\bullet$, and Fe^{2+} (iron), Cu^+ (copper) or other metallic ions participating in the Fenton reaction. In presence of transition metals, H_2O_2 can generate $OH^\bullet$ via $H_2O_2 + Fe^{2+}/Cu^+ \rightarrow OH^\bullet + OH^- + Fe^{3+}/Cu^{2+}$. Further beneficial improvements may include the consideration of an appropriate buffer, with the function of maintaining constant the pH of the system, and different acidity conditions, affecting both reaction rate constants, acid-base equilibria, and the final molecular yields (Roth and LaVerne 2011). Antioxidants are also only effective within a specific pH range. The explicit consideration of acid-base pairs, which according to Pastina and LaVerne (2001) are particularly relevant at longer time scales, along with the assessment of intermediate and high dose rates, may facilitate the enhancement of the predictions precision with respect to the experimental results, see figures 1, 2, and 4.

5. Conclusion

The objective of this study was to present the new features implemented in TRAX-CHEMxt, namely the ability to probe longer time scales (until s) and the introduction of biological species, monitoring the chemical effects under a wide range of radiation qualities, energies, LET values, and oxygenation conditions. The proven reliability of TRAX-CHEMxt depends on a computationally efficient algorithm, based on concentration distributions, which demonstrated to be of pivotal importance for the accurate treatment of the diverse reactants observed around the track centre of different particle qualities. A possible next application could be the analysis of the species yields dependencies on dose rate. The simulation of multiple tracks can be performed in both TRAX-CHEM and TRAX-CHEMxt, with some investigations already carried out within the MC framework (Castelli *et al* 2025). The simulations could assist in comprehending special and, to some extent, counterintuitive findings associated with FLASH experiments, as the observed decrease in H_2O_2 (Montay-Gruel *et al* 2019, Blain *et al* 2022). The code could also elucidate whether LET effects impact FLASH (Favaudon *et al* 2022). To conclude, a noteworthy potential application of TRAX-CHEMxt is in the context of precise chemotherapy. This promising treatment modality exploits the radiation-induced chemical activation of cancer prodrugs by primary water radicals, achieving a combined chemo-radio effect at the tumour site (Geng *et al* 2021). As a result, indirect and prodrug damages enhance the therapeutic effect, with an improved (selective) targeting and reduced toxicity. The current approach, predominantly performed with photon irradiations (Farrer *et al* 2022, Li *et al* 2022), can be therefore simulated, to both facilitate the understanding of the underlying mechanisms, and to test if different particle beams achieve the same outcomes.

Data availability statement

All data that support the findings of this study are included within the article (and any supplementary information files).

Acknowledgment

G Camazzola would like to thank the International Max Planck Research School for Quantum Dynamics in Physics, Chemistry and Biology, the Heidelberg Graduate School for Physics, and the Helmholtz Graduate School for Hadron and Ion Research for having supported his PhD research project. The publication is funded by the Open Access Publishing Fund of GSI Helmholtzzentrum für Schwerionenforschung.

Author contributions

G Camazzola 0000-0002-8204-7763
Conceptualization (lead), Data curation (lead), Formal analysis (lead), Methodology (lead), Software (lead), Validation (lead), Writing – original draft (lead)

D Boscolo 0000-0001-5709-4472
Conceptualization (supporting), Investigation (supporting), Resources (equal), Software (equal), Supervision (equal), Writing – review & editing (equal)

V Abram 0000-0002-3144-2317
Formal analysis (lead), Methodology (lead), Software (equal), Validation (supporting), Writing – review & editing (supporting)

E Scifoni 0000-0003-1851-5152
Conceptualization (equal), Methodology (supporting), Writing – review & editing (supporting)

A Dorn 0000-0002-8024-224X
Funding acquisition (lead), Project administration (lead), Resources (lead), Writing – review & editing (supporting)

M Durante 0000-0002-4615-553X
Funding acquisition (lead), Project administration (equal), Writing – review & editing (supporting)

M Krämer
Conceptualization (equal), Methodology (equal), Project administration (lead), Resources (equal), Software (lead), Supervision (lead), Writing – review & editing (equal)

M C Fuss 0000-0001-5332-6491
Conceptualization (lead), Investigation (equal), Methodology (lead), Project administration (lead), Resources (equal), Supervision (lead), Writing – review & editing (equal)

References

Adhikari S and Gopinathan C 1996 Oxidation reactions of a bovine serum albumin-bilirubin complex. A pulse radiolysis study *Int. J. Radiat. Biol.* **69** 89–98

Autsavapromporn N, Meesungnoen J, Plante I and Jay-Gerin J-P 2007 Monte Carlo simulation study of the effects of acidity and LET on the primary free-radical and molecular yields of water radiolysis—application to the Fricke dosimeter *Can. J. Chem.* **85** 214–29

Blain G *et al* 2022 Proton irradiations at ultra-high dose rate vs. conventional dose rate: strong impact on hydrogen peroxide yield *Radiat. Res.* **198** 318–24

Boscolo D, Krämer M, Durante M, Fuss M C and Scifoni E 2018 TRAX-CHEM: a pre-chemical and chemical stage extension of the particle track structure code TRAX in water targets *Chem. Phys. Lett.* **698** 11–18

Boscolo D, Krämer M, Fuss M C, Durante M and Scifoni E 2020 Impact of target oxygenation on the chemical track evolution of ion and electron radiation *Int. J. Mol. Sci.* **21** 424

Boyer P M and Hsu J T 1992 Experimental studies of restricted protein diffusion in an agarose matrix *AIChE J.* **38** 259–72

Burns W G and Sims H E 1981 Effect of radiation type in water radiolysis *J. Chem. Soc., Faraday Trans.* 1 **77** 2803–13

Camazzola G 2024 Fast and accurate: probing the homogeneous biochemical stage of radiation damage with the new TRAX-CHEMxt code *PhD Thesis* Heidelberg University

Cao X *et al* 2021 Quantification of oxygen depletion during FLASH irradiation in vitro and *in vivo Int. J. Radiat. Oncol. Biol. Phys.* **111** 240–8

Camazzola G, Boscolo D, Scifoni E, Dorn A, Durante M, Krämer M, Abram V and Fuss M C 2023 TRAX-CHEMxt: towards the homogeneous chemical stage of radiation damage *Int. J. Mol. Sci.* **24** 9398

Castelli L, Camazzola G, Fuss M C, Boscolo D, Krämer M, Tozzini V, Durante M and Scifoni E 2025 Probing spatiotemporal effects of intertrack recombination with a new implementation of simultaneous multiple tracks in TRAX-CHEM *Int. J. Mol. Sci.* **26** 571

Chappuis F, Grilj V, Tran H N, Zein S A, Bochud F, Bailat C, Incerti S and Desorgher L 2023 Modeling of scavenging systems in water radiolysis with Geant4-DNA *Phys. Med.* **108** 102549

Cobut V, Corbel C and Patau J P 2005 Influence of the pH on molecular hydrogen primary yields in $He^{2}+$ ion tracks in liquid water. A Monte Carlo study *Radiat. Phys. Chem.* **72** 207–15

Colliaux A, Gervais B, Rodriguez-Lafrasse C and Beuve M 2011 O_2 and glutathione effects on water radiolysis: a simulation study *J. Phys.: Conf. Ser.* **261** 012007

Davies M J 2016 Protein oxidation and peroxidation *Biochem. J.* **473** 805–25

El Khatib M *et al* 2022 Ultrafast tracking of oxygen dynamics during proton FLASH *Int. J. Radiat. Oncol. Biol. Phys.* **113** 624–34

Elliot A J and McCracken D R 1990 Computer modelling of the radiolysis in an aqueous lithium salt blanket: suppression of radiolysis by addition of hydrogen *Fusion Eng. Des.* **13** 21–27

Farrer N J, Higgins G S and Kunkler I H 2022 Radiation-induced prodrug activation: extending combined modality therapy for some solid tumours *Br. J. Cancer* **126** 1241–3

Favaudon V *et al* 2014 Ultrahigh dose-rate FLASH irradiation increases the differential response between normal and tumor tissue in mice *Sci. Transl. Med.* **6** 245ra93

Favaudon V, Labarbe R and Limoli C L 2022 Model studies of the role of oxygen in the FLASH effect *Med. Phys.* **49** 2068–81

Fleming A M and Burrows C J 2020 On the irrelevancy of hydroxyl radical to DNA damage from oxidative stress and implications for epigenetics *Chem. Soc. Rev.* **49** 6524–8

Gaigalas A K, Hubbard J B, McCurley M and Woo S 1992 Diffusion of bovine serum albumin in aqueous solutions *J. Phys. Chem.* **96** 2355–9

Ganesh H V S, Noroozifar M and Kerman K 2018 Epigallocatechin gallate-modified graphite paste electrode for simultaneous detection of redox-active biomolecules *Sensors* **18** 23

Gebicki S and Gebicki J M 1993 Formation of peroxides in amino acids and proteins exposed to oxygen free radicals *Biochem. J.* **289** 743–9

Geng J, Zhang Y, Gao Q, Neumann K, Dong H, Porter H, Potter M, Ren H, Argyle D and Bradley M 2021 Switching on prodrugs using radiotherapy *Nat. Chem.* **13** 805–10

Hawkins C L and Davies M J 2001 Generation and propagation of radical reactions on proteins *Biochim. Biophys. Acta* **1504** 196–219

Hawkins C L and Davies M J 2019 Detection, identification and quantification of oxidative protein modifications *J. Biol. Chem.* **294** 19683–708

Hu A, Qiu R, Wu Z, Zhang H and Li J 2022 CPU-GPU coupling independent reaction times method in NASIC and application in water radiolysis by FLASH irradiation *Biomed. Phys. Eng. Express* **8** 025015

Huie R 2003 NDRL/NIST solution kinetics database on the web (available at: https://kinetics.nist.gov/solution/)

Jin W and Chen H 2000 A new method of determination of diffusion coefficients using capillary zone electrophoresis (peak-height method *Chromatographia* **52** 17–21

Karle C *et al* 2024 Oxygen consumption measurements at ultra-high dose rate over a wide LET range *Med. Phys.* **52** 1323–34

Koch C J, Kim M M and Wiersma R D 2023 Radiation-chemical oxygen depletion depends on chemical environment and dose rate: implications for the FLASH effect *Int. J. Radiat. Oncol. Biol. Phys.* **117** 214–22

Kondo D *et al* 2025 Effect of FLASH dose-rate and oxygen concentration in the production of H_2O_2 in cellular-like media versus water: a Monte Carlo track-structure study *Phys. Med. Biol.* **70** 025014

Kosower N S and Kosower E M 1978 The glutathione status of cells *Int. Rev. Cytol.* **54** 109–60

Krämer M and Kraft G 1994 Calculations of heavy-ion track structure *Radiat. Environ. Biophys.* **33** 91–109

López-Alarcón C, Arenas A, Lissi E and Silva E 2014 The role of protein-derived free radicals as intermediaries of oxidative processes *Biomol. Concepts* **5** 119–30

Labarbe R, Hotoiu L, Barbier J and Favaudon V 2020 A physicochemical model of reaction kinetics supports peroxyl radical recombination as the main determinant of the FLASH effect *Radiother. Oncol.* **153** 303–10

Lai Y, Jia X and Chi Y 2021 Modeling the effect of oxygen on the chemical stage of water radiolysis using GPU-based microscopic Monte Carlo simulations, with an application in FLASH radiotherapy *Phys. Med. Biol.* **66** 025004
LaVerne J A 2000 Track effects of heavy ions in liquid water *Radiat. Res.* **153** 487–96
LaVerne J A and Pimblott S M 1993 Yields of hydroxyl radical and hydrated electron scavenging reactions in aqueous solutions of biological interest *Radiat. Res.* **135** 16–23
Leinisch F, Mariotti M, Rykaer M, Lopez-Alarcon C, Hägglund P and Davies M J 2017 Peroxyl radical- and photo-oxidation of glucose 6-phosphate dehydrogenase generates cross-links and functional changes via oxidation of tyrosine and tryptophan residues *Free Radical Biol. Med.* **112** 240–52
Li X, Sun H, Lu Y and Xing L 2022 Radiotherapy-triggered prodrug activation: a new era in precise chemotherapy *Med* **3** 600–2
Liu C-C and Gebicki J M 2012 Intracellular GSH and ascorbate inhibit radical-induced protein chain peroxidation in HL-60 cells *Free Radical Biol. Med.* **52** 420–6
Ma Y, Zhu C, Ma P and Yu K T 2005 Studies on the diffusion coefficients of amino acids in aqueous solutions *J. Chem. Eng. Data* **50** 1192–6
Meesat R, Sanguanmith S, Meesungnoen J, Lepage M, Khalil A and Jay-Gerin J-P 2012 Utilization of the ferrous sulfate (Fricke) dosimeter for evaluating the radioprotective potential of cystamine: experiment and Monte Carlo simulation *Radiat. Res.* **177** 813–26
Michaels H B and Hunt J W 1978 A model for radiation damage in cells by direct effect and by indirect effect: a radiation chemistry approach *Radiat. Res.* **74** 23–34
Mikkelsen R B and Wardman P 2003 Biological chemistry of reactive oxygen and nitrogen and radiation-induced signal transduction mechanisms *Oncogene* **22** 5734–54
Miyamoto S and Shimono K 2022 Estimation of the diffusion coefficients of small molecules by diffusion measurements with agar-gel and theoretical molecular modeling *Chem-Bio Inform. J.* **22** 13–20
Montay-Gruel P *et al* 2019 Long-term neurocognitive benefits of FLASH radiotherapy driven by reduced reactive oxygen species *Proc. Natl Acad. Sci. USA* **166** 10943–51
Nauser T, Koppenol W H and Schöneich C 2015 Protein thiyl radical reactions and product formation: a kinetic simulation *Free Rad. Biol. Med.* **80** 158–63
Neta P, Huie R E and Ross A B 1990 Rate constants for reactions of peroxyl radicals in fluid solutions *J. Phys. Chem. Ref. Data* **19** 413–513
Pastina B and LaVerne J A 1999 Hydrogen peroxide production in the radiolysis of water with heavy ions *J. Phys. Chem.* A **103** 1592–7
Pastina B and LaVerne J A 2001 Effect of molecular hydrogen on hydrogen peroxide in water radiolysis *J. Phys. Chem.* A **105** 9316–22
Piez K A and Eagle H 1958 The free amino acid pool of cultured human cells *J. Biol. Chem.* **231** 533–45
Plante I 2021 A review of simulation codes and approaches for radiation chemistry *Phys. Med. Biol.* **66** 03TR02
Ramos-Méndez J *et al* 2020 Independent reaction times method in Geant4-DNA: implementation and performance *Med. Phys.* **47** 5919–30
Romero C M, Trujillo G P, Verissimo L M, Esteso M A, Ramos M L and Ribeiro A C 2019 Limiting diffusion coefficients of α,ω-amino acids in water and in sodium chloride aqueous solutions at 298.15 K *Eur. Phys. J.* E **42** 94
Roth O and LaVerne J A 2011 Effect of pH on H_2O_2 production in the radiolysis of water *J. Phys. Chem.* A **115** 700–8
Schuessler H and Davies J V 1983 Radiation-induced reduction reactions with bovine serum *Int. J. Radiat. Biol.* **43** 291–301
Shamim M and Baki S M A 1980 Diffusion measurements in aqueous L-ascorbic acid solutions *Aust. J. Chem.* **33** 1857–61
Shin W-G *et al* 2024 Investigation of hydrogen peroxide yields and oxygen consumption in high dose rate irradiation: a TOPAS-nBio Monte Carlo study *Phys. Med. Biol.* **70** 015012
Soriano A N, Dollente K G, Tabaquero R J and Adornado A P 2018 Estimation of diffusion coefficients of ascorbate-based ions at infinite dilution through electrolytic conductivity measurements *IOP Conf. Ser.: Earth Environ. Sci.* **191** 012028
Spitz D R, Buettner G R, Petronek M S, St-Aubin J J, Flynn R T, Waldron T J and Limoli C L 2019 An integrated physico-chemical approach for explaining the differential impact of FLASH versus conventional dose rate irradiation on cancer and normal tissue responses *Radiother. Oncol.* **139** 23–27
Stricks W and Kolthoff I M 1952 Polarography of glutathione *J. Am. Chem. Soc.* **74** 4646–53
Tan H S, Teo K B K, Dong L, Friberg A, Koumenis C, Diffenderfer E and Zou J W 2023 Modeling ultra-high dose rate electron and proton FLASH effect with the physicochemical approach *Phys. Med. Biol.* **68** 145013
Tang B, Chong K, Massefski W and Evans R 2022 Quantitative interpretation of protein diffusion coefficients in mixed protiated-deuteriated aqueous solvents *J. Phys. Chem.* B **126** 5887–95
Thomas W, Sunnerberg J, Reed M, Gladstone D J, Zhang R, Harms J, Swartz H M and Pogue B W 2024 Proton and electron ultrahigh-dose-rate isodose irradiations produce differences in reactive oxygen species yields *Int. J. Radiat. Oncol. Biol. Phys.* **118** 262–7
Torres J F, Komiya A, Okajima J and Shigenao M 2012 Measurement of the molecular mass dependence of the mass diffusion coefficient in protein aqueous solutions *DDF* **326** 452–8
Tran H N, Chappuis F, Incerti S, Bochud F and Desorgher L 2021 Geant4-DNA modeling of water radiolysis beyond the microsecond: an on-lattice stochastic approach *Int. J. Mol. Sci.* **22** 6023
Traut T W 1994 Physiological concentrations of purines and pyrimidines *Mol. Cell. Biochem.* **140** 1–22
von Sonntag C 2006 *Free-Radical-Induced DNA Damage and Its Repair: A Chemical Perspective* (Springer)
Wälzlein C, Krämer M, Scifoni E and Durante M 2014 Advancing the modeling in particle therapy: from track structure to treatment planning *Appl. Radiat. Isot.* **83** 171–6
Wang Z, Kriegs H and Wiegand S 2012 Thermal diffusion of nucleotides *J. Phys. Chem.* B **116** 7463–9
Wardman P 2022 Approaches to modeling chemical reaction pathways in radiobiology *Int. J. Radiat. Biol.* **98** 1399–413
Wardman P and von Sonntag C 1995 Kinetic factors that control the fate of thiyl radicals in cells *Methods Enzymol.* **251** 31–45
Wasselin-Trupin V, Baldacchino G, Bouffard S and Hickel B 2002 Hydrogen peroxide yields in water radiolysis by high-energy ion beams at constant LET *Radiat. Phys. Chem.* **65** 53–61
Winterbourn C C 2016 Revisiting the reactions of superoxide with glutathione and other thiols *Arch. Biochem. Biophys.* **595** 68–71
Yu M, Silva T C, van Opstal A, Romeijn S, Every H A, Jiskoot W, Witkamp G-J and Ottens M 2019 The investigation of protein diffusion via H-cell microfluidics *Biophys. J.* **116** 595–609
Zhu H, Li J, Deng X, Qiu R, Wu Z and Zhang H 2021 Modeling of cellular response after FLASH irradiation: a quantitative analysis based on the radiolytic oxygen depletion hypothesis *Phys. Med. Biol.* **66** 185009